Crystal Plasticity Based Fe Model for Understanding Microstructural Effects on Creep and Dwell Fatigue in Ti-6242

Gayathri Venkataramani
Graduate Research Associate

Dhyanjyoti Deka
Graduate Research Associate

Somnath Ghosh
John B. Nordholt Professor

Computational Mechanics Research Laboratory,
Department of Mechanical Engineering,
The Ohio State University,
Columbus, OH 43202

This paper is aimed at identifying key microstructural parameters that play important roles in the failure initiation of polycrystalline Ti-6242 *subjected to creep and dwell loading. A finite element model, incorporating rate dependent elastocrystal plasticity, is developed for analyzing evolving variables in material microstructure. The crystal plasticity parameters are characterized by a combination of microtesting, orientation imaging microscopy, computational simulations, and minimization process involving Genetic algorithms (Ga). Accurate phase volume fractions and orientation distributions that are statistically equivalent to those observed in orientation imaging microscope scans are incorporated in the computational model of polycrystalline* Ti-6242 *for constant strain rate, creep, and dwell tests. The computational model is used for the identification of possible microstructural variables that may result in local crack initiation. Basal normal stress, equivalent plastic strain, and stress in loading direction are considered as candidate parameters, of which the former is chosen as most probable from results of creep and dwell experiments and simulations. Creep induced load shedding phenomena is observed to lead to high value stresses that cause failure. The role of grain orientation with respect to the loading axis and misorientation with its neighbors, in causing load shedding and stress localizations is explored.* [DOI: 10.1115/1.2204942]

Keywords: crystal plasticity, finite element analysis, Ti-6242, creep, dwell fatigue

1 Introduction

Dwell fatigue in two-phase α/β titanium alloys has drawn significant attention due to the early failure of structural components at room temperature when subjected to dwell cycle loading. Experimental studies on dwell fatigue and normal fatigue have shown that dwell specimens show a marked reduction in the number of cycles to failure compared with the pure fatigue specimens [1]. Prior research on α/β titanium alloys have attributed the dwell sensitivity to deleterious mechanism of "cold-creep" or strain accumulation [2–5], in which significant time-dependent strain accumulates under static applied stresses that are lower than or equal to yield strength. These observations suggest that time-dependent strain accumulation due to creep is a critical factor in understanding failure mechanisms in dwell fatigue.

The time-dependent plastic deformation in Ti alloys, on the other hand, has considerable dependence on the grain orientation due to the low symmetry of the predominant hcp α phase. Experiments employing electron back scattered diffraction (EBSD) technique in scanning electron microscopy or orientation imaging microscopy (OIM) have shown [6] that the relative strength of neighboring grains are highly dependent on the orientation of basal planes with respect to the axis of loading. This is because in the [0001] orientation, $\langle c+a\rangle$ dislocation slip on pyramidal slip systems are activated which have a much higher critical resolved shear strength (CRSS) than the $\langle a\rangle$ type slip on basal or prismatic planes. Large local stress concentrations are found to develop in these $\langle c+a\rangle$ oriented grains due to local load shedding from neighboring softer $\langle a\rangle$ oriented grains. Hence the local grain morphology and consequently load shedding between grains are of considerable importance in crack initiation in Ti alloys.

Examinations of crack initiation site in normal fatigue experiments [1] have shown a high degree of local plastic strain accumulation than that observed in dwell fracture initiation site. The dwell fracture initiation site was similar to those observed for the static loading condition at higher peak stress (~95% of yield strength) and the fracture site showed little evidence of ductility. Though the dwell and creep experiments show significant time-dependent strain accumulation, the failure mode has been observed [1] to be faceted and brittle. This points to the fact that stress localizations caused by significant stress redistribution between grains of different strengths leads to crack initiation and subsequent failure in polycrystalline Ti-6242 (see Table 1 for composition). This has also been observed in the dwell fatigue and creep experiments [7,8], which have been used to study the mode of failure in polycrystalline Ti-6242. Also, examinations of fracture surfaces from dwell fatigue experiments [9] have shown that fracture facets correspond to α colonies with the fracture plane lying on or close to basal plane. These experimental observations point to the fact that the stress normal to the basal plane and stress distribution between regions of different strengths plays a critical role in dwell fatigue and creep failure in two-phase α/β titanium alloys.

The study of dwell fatigue phenomena in two-phase Ti-6242 alloys requires special focus on creep due to time-dependent accumulation of plastic strain and the load shedding phenomena of stress redistribution consistent with grain orientation and morphology. To effectively model these phenomena, a time-dependent large strain finite element (FE) model has been developed by the authors in [10] and in the present work. Ti-6242 alloy consists of transformed β colonies in a matrix of equiaxed primary α grains as shown in Fig. 1(*a*). The model incorporates rate-dependent anisotropic elastic-crystal plasticity constitutive models for the dif-

Contributed by the Materials Division of ASME for publication in the JOURNAL OF ENGINEERING MATERIALS AND TECHNOLOGY. Manuscript received October 17, 2005; final manuscript received February 28, 2006. Review conducted by Kenneth Gall.

Table 1 Chemical composition of Ti-6242

Alloy	Al (wt %)	Mo (wt %)	Sn (wt %)	Zr (wt %)	Si (wt %)	O (wt %)	N (wt %)	Ti (wt %)
Ti-6242	6.01	1.96	1.96	4.01	0.10	0.131	0.012	85.82

ferent phases in this material. Details of the microstructural morphology are accounted for in the model, through accurate phase volume fractions, and orientation distributions that are statistically equivalent to those observed in orientation imaging microscopy (OIM) scans. Material properties for each of the constituent phases and individual slip systems in the crystal plasticity model are calibrated by a genetic algorithm (GA) based optimization scheme. The crystal plasticity parameters, calibrated from constant strain rate and creep tests on single colony crystals, are adjusted to account for the size effects in the polycrystalline microstructure. In addition, tension-compression asymmetry is also accounted for in the slip system variables, to reflect experimental observations. Finally, a homogenized model of the $\alpha+\beta$ phase colony regions in the Ti-6242 microstructure has been developed for incorporation in the FE model. The computational model has been validated by comparing the results of simulation with those from constant strain rate and creep tests on polyphase-polycrystalline Ti-6242. Details of the development of this model are discussed in a preceding paper [10].

This paper is aimed at using the finite element model (FEM) based computational model in [10] to investigate key microstructural parameters and evolving variables that play a role in instigating failure in polycrystalline Ti-6242 subjected to dwell and creep loading. Motivated by experimental observations and previous studies in [1,10–12], stress normal to the basal planes (basal normal stress), stress in the loading direction, and the equivalent plastic strain are chosen as probable evolving variables which may contribute to the nucleation of cracks in polycrystalline Ti -6242 in creep and dwell loading. The critical variables are identified from a comparative study of the results of creep and dwell simulations, with creep and dwell fatigue experiments that have been performed in [7,8]. Subsequently, critical microstructural parameters, e.g., orientation and misorientation distributions that contribute to the evolution of these variables to cause local failure are deciphered from the results of simulations and assessment of the various morphological distributions. The observations of this study may be incorporated in a failure initiation criterion that can account for distributions of critical microstructural variables.

2 Material Description

An optical micrograph of a forged α/β Ti-6242 material is shown in Fig. 1(*a*). The microstructure consists of regions of transformed β colonies in a matrix of equiaxed primary α grains with a hcp crystalline structure. The transformed β colonies consist of alternating α (hcp) and β (bcc) laths as shown in Fig. 1(*b*). For the hcp lattice structure, the material basis vectors are denoted by a set of nonorthogonal base vectors $\{\boldsymbol{a}_1,\boldsymbol{a}_2,\boldsymbol{a}_3,\mathbf{c}\}$ as discussed in [11,13]. As shown in Fig. 2(*a*), the hcp crystals consist of five different families of slip systems, namely, the basal $\langle a\rangle$, prismatic $\langle a\rangle$, pyramidal $\langle a\rangle$, first-order pyramidal $\langle c+a\rangle$, and second-order pyramidal $\langle c+a\rangle$ with a total of 30 possible slip systems. A transversely isotropic elastic response is assumed for these crystals with five independent constants. The bcc crystal system consists of three different slip families $\langle 111\rangle$ $\{110\}$, $\langle 111\rangle$ $\{112\}$, and $\langle 111\rangle$ $\{123\}$ with a total of 48 slip systems, defined by three lattice vectors in the Cartesian coordinate system $\{\boldsymbol{e}_1^c,\boldsymbol{e}_2^c,\boldsymbol{e}_3^c\}$ as shown in Fig. 2(*b*). A cubic symmetric elastic matrix is assumed for the bcc material with three independent constants.

The volume fraction of the transformed β phase in the Ti-6242 material microstructure is 30% for the specimens analyzed. Within the transformed β colonies, the α and β lamellae are experimentally observed to have volume fractions of approxi-

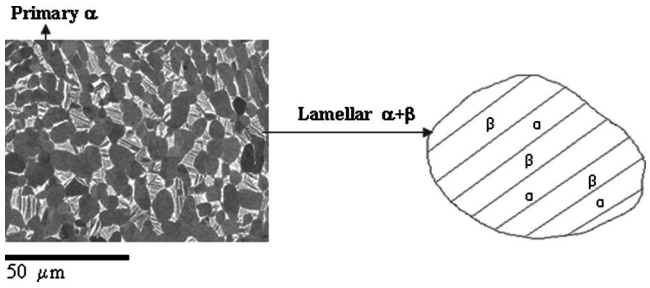

Fig. 1 (*a*) Microstructure of a forged $\alpha+\beta$ Ti-6242 alloy consisting of transformed β (dark phase) colonies in a matrix of equiaxed primary α grains (light phase) and (*b*) schematic of a constituent transformed β colony

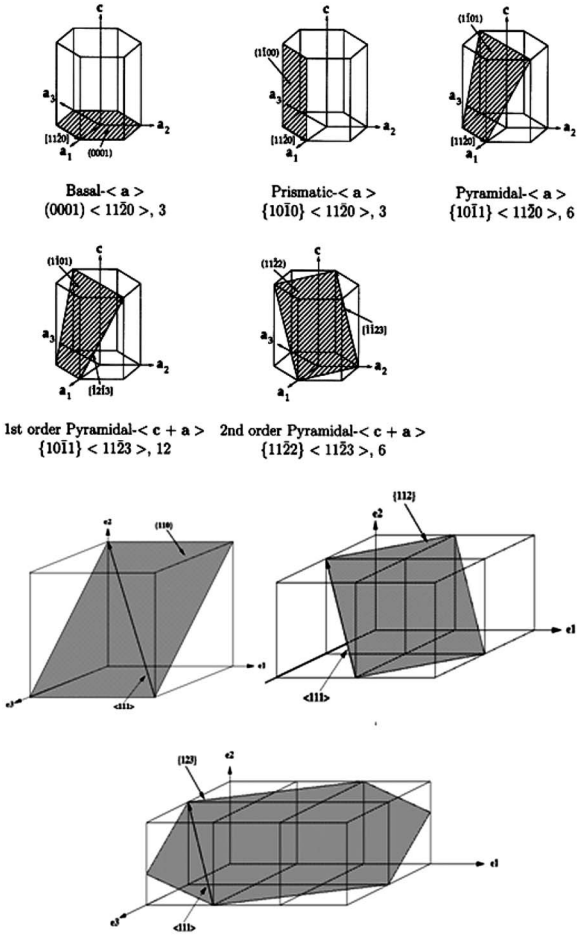

Fig. 2 Schematic diagrams showing (*a*) the nonorthogonal basis and slip systems in a hcp crystal and (*b*) the orthogonal basis and slip systems in bcc crystals

mately 88% and 12%, respectively, in [14]. The orientations of α and β lamellae follow a Burgers orientation relationship [15], expressed as $(101)_\beta \| (0001)_\alpha, [1\bar{1}\bar{1}]_\beta \| [2\bar{1}\bar{1}0]_\alpha$. This relation brings the hcp $\boldsymbol{a}_1$ ($[2\bar{1}\bar{1}0]$) slip direction into coincidence with the bcc $\boldsymbol{b}_1$ slip direction. OIM images [1,14] have shown that there is a very small misalignment of ~0.56 deg between the $\boldsymbol{a}_1$ and $\boldsymbol{b}_1$ slip directions for this alloy. However, there is a significant misalignment between the α phase $\boldsymbol{a}_2$ ($[\bar{1}2\bar{1}0]$) and β phase $\boldsymbol{b}_2$ slip directions, and also between the $\boldsymbol{a}_3$ ($[\bar{1}\bar{1}20]$) and all $\langle 111\rangle_\beta$ directions in the β phase. Consequently, the ease of α/β slip transmission for $\boldsymbol{a}_1, \boldsymbol{a}_2$, and $\boldsymbol{a}_3$ basal and prismatic slips varies significantly.

In [10], a homogenized equivalent crystal model of the $\alpha+\beta$ or transformed β phase colony regions has been developed. The model consists of 78 slip systems, of which 30 correspond to hcp (secondary α) and 48 correspond to bcc slip systems, with the alignment of α and β lamellae following the Burger's orientation relationship. The equivalent crystal is constructed based on the assumptions of the Taylor model, where a uniform deformation gradient F_{ij} is assumed for the two phases [16]. In [10], the equivalent transformed β model has been shown to yield reasonably accurate predictions of the overall stress-strain behavior and slip system evolution, in comparison with a detailed FE model containing explicit representation of the α and β phases. The equivalent model is compact, and is hence convenient to use for representing the transformed β phase in a FE model of Ti-6242.

3 The Constitutive Model

The deformation behavior of individual phases of the Ti-6242 microstructure is modeled using a rate-dependent, isothermal, elastic-plastic, finite strain, crystal plasticity formulation, following [11,13,17–19]. The general framework for the crystal plasticity formulation is taken to be the same for both the hcp and bcc phases, with the only difference introduced in the hardening laws. The stress-strain relation in this model is written in terms of the second Piola-Kirchoff stress $\mathbf{S}(=\det \mathbf{F}^e \mathbf{F}^{e-1} \boldsymbol{\sigma} \mathbf{F}^{e-T})$ and the work conjugate Lagrange-Green strain tensor $\mathbf{E}^e\left(=\frac{1}{2}\{\mathbf{F}^{eT}\mathbf{F}^e - \mathbf{I}\}\right)$ as

$$\mathbf{S} = \boldsymbol{C} : \mathbf{E}^e \tag{1}$$

where $\boldsymbol{C}$ is the fourth-order anisotropic elasticity tensor, $\boldsymbol{\sigma}$ is the Cauchy stress tensor, and $\mathbf{F}^e$ is the elastic deformation gradient defined by the relation

$$\mathbf{F}^e \equiv \mathbf{F}\mathbf{F}^{p^{-1}}, \quad \det \mathbf{F}^e > 0 \tag{2}$$

$\mathbf{F}$ and $\mathbf{F}^p$ are the deformation gradient and its plastic component, respectively, with the incompressibility constraint $\det \mathbf{F}^{\mathrm{P}} = 1$. The flow rule governing evolution of plastic deformation is expressed in terms of the plastic velocity gradient as

$$\mathbf{L}^p = \dot{\mathbf{F}}^p \mathbf{F}^{p^{-1}} = \sum_\alpha \dot{\gamma}^\alpha \mathbf{s}_0^\alpha \tag{3}$$

where the αth slip system Schmid tensor is expressed as $\mathbf{s}_0^\alpha \equiv \mathbf{m}_0^\alpha \otimes \mathbf{n}_0^\alpha$ in terms of the slip direction $\mathbf{m}_0^\alpha$ and slip plane normal $\mathbf{n}_0^\alpha$ in the reference configuration. The plastic shearing rate $\dot{\gamma}^\alpha$ on the αth slip system is given by the power law relation [17], expressed as

$$\dot{\gamma}^\alpha = \dot{\tilde{\gamma}} \left| \frac{\tau^\alpha}{g^\alpha} \right|^{1/m} \mathrm{sgn}(\tau^\alpha), \quad \tau^\alpha \equiv (\mathbf{C}^e : \mathbf{S}) \cdot \mathbf{s}_0^\alpha \tag{4}$$

Here $\dot{\tilde{\gamma}}$ is the reference plastic shearing rate, τ^α and g^α are the αth slip system resolved shear stress and the slip system deformation resistance, respectively, m is the material rate sensitivity parameter, and $\mathbf{C}^e$ is the elastic stretch. The slip system resistance is taken to evolve as

$$\dot{g}^\alpha = \sum_{\beta=1}^{\mathrm{nslip}} h^{\alpha\beta} |\dot{\gamma}^\beta| = \sum_\beta q^{\alpha\beta} h^\beta |\dot{\gamma}^\beta| \tag{5}$$

where $h^{\alpha\beta}$ corresponds to the strain hardening rate due to self and latent hardening, h^β is the self-hardening rate and $q^{\alpha\beta}$ is a matrix describing the latent hardening. For the hcp phase, the evolution of the self-hardening rate is governed by the relation [20]

$$h^\beta = h_0^\beta \left| 1 - \frac{g^\beta}{g_s^\beta} \right|^r \mathrm{sgn}\left(1 - \frac{g^\beta}{g_s^\beta}\right), \quad g_s^\beta = \tilde{g}\left(\frac{\dot{\gamma}^\beta}{\dot{\tilde{\gamma}}}\right)^n \tag{6}$$

where h_0^β is the initial hardening rate, g_s^β is the saturation slip deformation resistance, and r, $\tilde{g}$, and n are the slip system hardening parameters. For bcc materials, the evolution of the self-hardening rate is given as [21], as

$$h^\beta = h_s^\beta + \mathrm{sech}^2\left[\left(\frac{h_0^\beta - h_s^\beta}{\tau_s^\beta - \tau_0^\beta}\right)\gamma_a\right](h_0^\beta - h_s^\beta), \quad \gamma_a = \int_0^t \sum_{\beta=1}^{\mathrm{nslip}} |\dot{\gamma}^\beta| \tag{7}$$

where h_0^β and h_s^β are the initial and asymptotic hardening rates, τ_s^β represents the saturation value of the shear stress when $h_s^\beta = 0$, and γ_a is a measure of total plastic shear. For modeling cyclic deformation it is important to include kinematic hardening. This has been done by including a backstress in the power law Eq. (4) as in [11,19]. Consequently, the rate of crystallographic slip on a particular slip system is expressed as

$$\dot{\gamma}^{(\alpha)} = \dot{\gamma}_0 \left| \frac{\tau^{(\alpha)} - \chi^{(\alpha)}}{g^{(\alpha)}} \right|^{1/m} \mathrm{sgn}(\tau^{(\alpha)} - \chi^{(\alpha)}) \tag{8}$$

where $\chi^{(\alpha)}$ is the backstress on the αth slip system. An Armstrong-Frederick type nonlinear kinematic hardening rule is chosen for the evolution of backstress as

$$\dot{\chi}^{(\alpha)} = c\,\dot{\gamma}^{(\alpha)} - d\chi^{(\alpha)} |\dot{\gamma}^{(\alpha)}| \tag{9}$$

Here c and d are the direct hardening and the dynamic recovery coefficients, respectively.

The homogenized constitutive relation for the equivalent model of the transformed β phase involves the calculation of the second Piola-Kirchoff stress tensors $S_{ij}^{\mathrm{hcp}}(F_{kl}, \dot{\gamma}_{\mathrm{hcp}}^\alpha)$ and $S_{ij}^{\mathrm{bcc}}(F_{kl}, \dot{\gamma}_{\mathrm{bcc}}^\alpha)$ for the 30 hcp slip systems in the α phase and 48 bcc slip systems in the β phases separately using Eqs. (1)–(9). The corresponding true stress tensors in each of the phases are calculated by the transformation

$$\sigma_{ij}^{\mathrm{hcp}}(F_{kl}, F_{mn}^{\mathrm{hcp}(e)}) = \frac{1}{\det F_{mn}^{\mathrm{hcp}(e)}} F_{ik}^{\mathrm{hcp}(e)} S_{kl}^{\mathrm{hcp}} F_{jl}^{\mathrm{hcp}(e)} \quad \text{and}$$

$$\sigma_{ij}^{\mathrm{bcc}}(F_{kl}, F_{mn}^{\mathrm{bcc}(e)}) = \frac{1}{\det F_{mn}^{\mathrm{bcc}(e)}} F_{ik}^{\mathrm{bcc}(e)} S_{kl}^{\mathrm{bcc}} F_{jl}^{\mathrm{bcc}(e)} \tag{10}$$

where $F_{ij}^{\mathrm{hcp}(e)}$ and $F_{ij}^{\mathrm{bcc}(e)}$ are the elastic deformation gradients in Eq. (2). Finally, the true stress tensor in the homogenized material model of the equivalent crystal is obtained by the rule of mixtures, where the phase volume fractions are taken as the weights in the weighted averaging of formula. The corresponding homogenized stress is expressed as

$$\boldsymbol{\sigma}_{ij}^{\mathrm{tran}-\beta} = v_f^{\mathrm{hcp}} \boldsymbol{\sigma}_{ij}^{\mathrm{hcp}}(F_{ij}, F_{kl}^{\mathrm{hcp}*}) + v_f^{\mathrm{bcc}} \boldsymbol{\sigma}_{ij}^{\mathrm{bcc}}(F_{ij}, F_{kl}^{\mathrm{bcc}*}) \tag{11}$$

where v_f^{hcp} and v_f^{bcc} are the respective phase volume fractions.

The crystal plasticity model is incorporated in the commercial finite element code MSC MARC [22] using the user defined material routine HYPELA2. An implicit time integration scheme proposed in [17,20] has been employed to integrate the crystal plasticity Eqs. (1)–(9). Known deformation variables like the deformation gradient $\mathbf{F}(t)$, the plastic deformation gradient $\mathbf{F}^{\mathrm{p}}(t)$, and the slip system deformation resistance $S^\alpha(t)$ at time t, and the deformation

Table 2 Values of the initial deformation resistance g_o^γ for secondary α (hcp) and β (bcc) laths in transformed β regions and primary α grains accounting for size effects

Tensile (secondary α)						
Parameter	a_1 basal	a_2 basal	a_3 basal	a_1 prismatic	a_2 prismatic	a_3 prismatic
Modified g_o^α	412 MPa	422 MPa	382 MPa	372 MPa	362 MPa	382 MPa
χ	1.45	1.34	1.57	1.55	1.72	1.59

Compressive (secondary α)			
Parameter	a_1 basal	a_2 basal	a_3 basal
g_o^α	458 MPa	487 MPa	478 MPa
size factor χ	1.18	1.08	1.05

β phase					
Parameter	{101}	{112} soft	{112} hard	{123} soft	{123} hard
g_o^α	445 MPa	404.63 MPa	424.82 MPa	395.67 MPa	446.28 MPa
size factor χ	1.78	1.93	1.85	1.97	1.78

Primary α			
	Basal $\langle a \rangle$ system	Prismatic $\langle a \rangle$ system	Pyramidal $\langle c+a \rangle$ system
Tensile	365 MPa	345 MPa	619.8 MPa
Compressive	428 MPa	463 MPa	758.8 MPa

gradient $\mathbf{F}(t+\Delta t)$ at $t+\Delta t$ are passed to the material update routine in HYPELA2. The integration algorithm in the HYPELA2 subroutine updates stresses, plastic strains, and all slip system internal variables to the end of the time step at $t+\Delta t$. Discussion of this implementation in ABAQUS using UMAT material update routine has been presented in [11,19].

4 Material Parameters

Material parameters are systematically calibrated from experimental results in [10] by using a genetic algorithm (GA) based technique [19,23], in which a minimization of the least square of the difference between the experimental and simulation material properties is performed. The material parameters calibrated include (a) the set $C_{\alpha\beta}$ $(\alpha=1,\ldots,6,\beta=1,\ldots,6)$, of anisotropic elastic stiffness components, (b) the set of flow related parameters, $\tilde{\gamma}, g^\alpha, m$, and (c) the set of hardening evolution related parameters $h_o, h_s, \tau_0, \tau_s, r, n, g$ in the hcp and bcc phases as discussed in Eqs. (1)–(7). All the calibrations have been validated by comparing the corresponding single colony stress-strain plots of experimental and computational results [10] and excellent agreement has been demonstrated. The calibrated values of crystal plasticity parameters are presented in [10]. The kinematic hardening parameters in Eqs. (8) and (9) are chosen to be $c=500$ MPa and $d=100$ MPa for all the slip systems from [11].

The α/β laths in the transformed β phase and also the primary α grains in the polycrystalline Ti-6242 are much finer than the single colony samples or the single crystal α Ti-6Al-4V crystals of [14], used in the calibration process. Strengthening with smaller lath size in β processed Ti-6Al-4V has been experimentally observed in [12] and the same effects prevail in Ti-6242, making the in situ phases relatively stronger. Consequently, crystal plasticity parameters calibrated from single crystal and single colony tests are modified in [10] to incorporate *Hall-Petch* or size effects prior to their use in the polycrystalline models. Consequently, the initial slip system deformation resistance g_o^γ is modified by a size factor χ. For the secondary α in the transformed β colonies, the size factor χ for individual slip systems are evaluated from polycrystalline constant strain rate results in tension and the values g_o^γ and χ values are reported in Table 2. The corresponding values for the primary α regions are also shown in Table 2.

Significant tension/compression asymmetry has been observed in the single colonies of α/β Ti6242 in the experimental studies of [1,14]. This behavior has been attributed to one or a combination of a number of mechanisms, viz. residual stresses in single colony due to growth process, elastic stress fields at the α/β interface aiding or impairing slip transmission, effects on the mobility of $\langle \boldsymbol{a} \rangle$ type dislocations in the α phase, and effects on the mobility of dislocations in the β phase and differing slip transmission mechanisms based on the direction of loading. Calibration of the crystal plasticity parameters in [10] account for tension-compression asymmetry in each slip system. For example, the $\langle 111 \rangle \{110\}$ system is symmetric with respect to the direction of shear along the $\langle 111 \rangle$ axis whereas the $\langle 111 \rangle \{112\}$ and $\langle 111 \rangle \{123\}$ are not. Slip in the latter two systems along one direction has a lower shear strength and higher energetic maximum than slip in the reverse direction [24]. Consequently, along each slip direction, a "hard direction" is designated which has a higher shear strength and energetic maximum compared to its reverse "soft direction." Crystal plasticity parameters are calibrated separately for the hard and soft directions of the $\langle 111 \rangle \{110\}$, $\langle 111 \rangle \{112\}$, and $\langle 111 \rangle \{123\}$ systems.

5 Crystallographic Orientation Distribution in the FE Model

Each element in the FE representation of polycrystalline Ti-6242 aggregate, shown in Fig. 3(*c*), represents a single globular α grain or a transformed β grain ($\alpha+\beta$ colony). The deformation and creep response has been observed to be sensitive to the overall texture in [11,19]. Consequently for physically meaningful simulations, it is important to assign appropriate crystallographic orientations to the elements in the FE model, that are statistically equivalent to those obtained from orientation imaging microscopy (OIM). OIM involves electron back-scattered diffraction (EBSD) in scanning electron microscopy, and a typical OIM map for the forged Ti-6242 sample is shown in Fig. 3(*d*). Texture assignment to the FE model involves three main steps delineated as: (a) orientation assignment using the orientation probability assignment method (OPAM); (b) misorientation assignment using the misorientation probability assignment method (MPAM); and (c) microtexture assignment using the microtexture probability assignment method (MTPAM). These three steps have been developed in [10] and are described briefly in this section. It should be noted that the orientation distributions (Euler angles) assigned by these methods

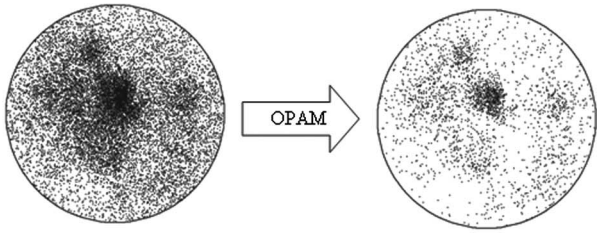

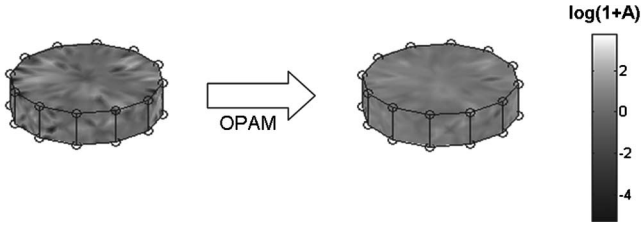

Fig. 4 Comparison of crystallographic texture using Rodrigue's vector representation (*a*) from orientation imaging microscopy, and (*b*) from OPAM based simulations. *A* is the density of Rodrigue's vector points.

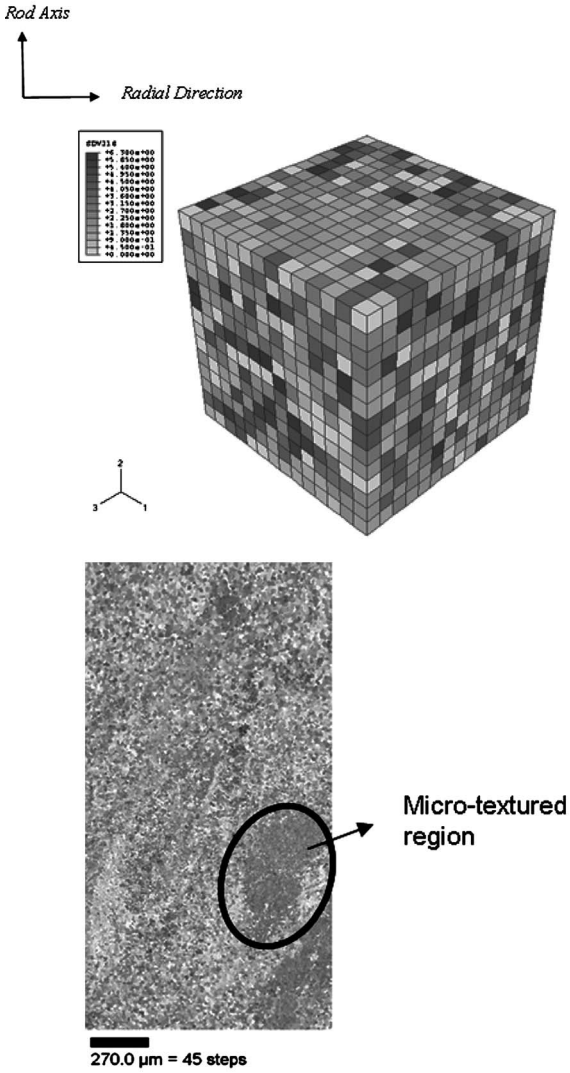

Fig. 3 Orientation assignment to the finite element mesh: (*a*) experimentally observed (0001) pole figure with 14,799 points; (*b*) OPAM simulated pole figure with 2744 points; (*c*) FE model showing element orientations; and (*d*) OIM image produced by EBSD scan

are for hcp orientations only. The bcc orientations are calculated from the secondary hcp orientations using the Burgers orientation relation.

The statistically equivalent orientations assignment using the orientation probability assignment method or OPAM is developed and discussed in [19,25]. In this method, crystallographic orientations, represented by Euler angles, are first generated from transformed pole figures. In these figures, points in discretized regions of the projected plane are extracted from contour plots of the pole figures in x-ray diffraction analysis. This process generally generates a number of Euler angles (14,799 in Fig. 3(*a*)) that are considerably larger than the assignable orientations to the FE model with smaller number of elements. Consequently, the OPAM assigns orientations with similar probability density distributions of the crystallographic orientations to the finite element mesh. Experimentally measured (0001) pole figures with 14,799 orientations are compared with 2744 simulated orientations assigned by OPAM in Figs. 3(*a*) and 3(*b*). The corresponding logarithmic plot of Rodrigues vector density, discussed in [26], is shown in Fig. 4 for the experimental and simulated crystallographic orientations. It is obvious that all textures are adequately represented in the simulated model by OPAM.

Computational studies in [19] show that large stresses and plastic strain concentrations can arise at grain boundaries that exhibit large values of misorientation with its neighbors. Consequently, a misorientation distribution (MOD) that is statistically equivalent to that observed in OIM scans, is assigned in addition to the OPAM based orientation distribution. The misorientation between two neighboring grains A and B is measured in terms of a rotation axis vector $\bar{n}$ and a misorientation angle θ, as described in [10,19]. The axis $\bar{n}$ represents a common crystallographic lattice or slip direction for both crystal lattices. The angle θ is the rotation about $\bar{n}$ required to bring the two crystal lattices into coincidence. The misorientation angle θ between two neighboring grains is expressed quantitatively as (see [27])

$$\theta = \min \left| \cos^{-1} \left\{ \frac{\mathrm{tr}(\mathbf{g}_A \mathbf{g}_B^{-1} \mathbf{O} - \mathbf{1})}{2} \right\} \right| \tag{12}$$

where $\boldsymbol{g_A}$ and $\boldsymbol{g_B}$ are the orientation matrices of grains A and B, respectively, and $\mathbf{O}$ is the crystal symmetry operator. Considering that there are 12 identical rotation operations in hexagonal symmetry, the misorientation of the two lattices can be described by 12 different symmetrically equivalent rotations. The minimum rotation angle is chosen as the misorientation angle. Figure 5(*a*) shows the OIM data of volume fractions of grains with misorientation angles between 0 deg and 90 deg, divided into ten bins with a 10 deg increment angle between the neighboring bins. In the misorientation probability assignment or MPAM, the number fraction of grains with misorientation angles observed in the OIM data (Fig. 5(*a*)) is compared with the simulation data, starting with the distribution generated by OPAM. Grain pairs, which contribute to bins showing the largest difference between OIM and simulated data, are moved around in an iterative manner until a good match is obtained with the experimental data. The method of producing equivalent MOD by MPAM is detailed in [10]. The final misorientation distribution obtained by the OPAM+MPAM method is shown in Fig. 5(*b*), which illustrates the good match between the simulated and experimental misorientation distributions.

The orientation and misorientation probability assignment (OPAM+MPAM) method alone, does not guarantee spatial arrangement of the grains in the model to form the contiguities or microtextures that are observed in the OIM maps, e.g., in Fig. 3(*d*). Woodfield et al. [9] have observed that specimens of α/β processed Ti-6242 that contain large microtextured regions of primary α colonies, have significantly shorter life than those with no

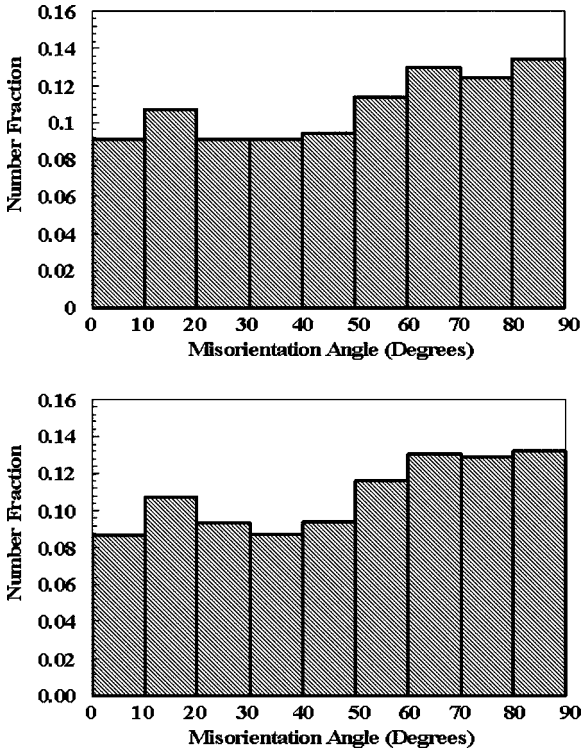

Fig. 5 Histograms of the number fraction of experimental and simulation misorientation distribution: (a) experimental misorientation distribution; (b) simulated MOD with OPAM+MPAM based orientation

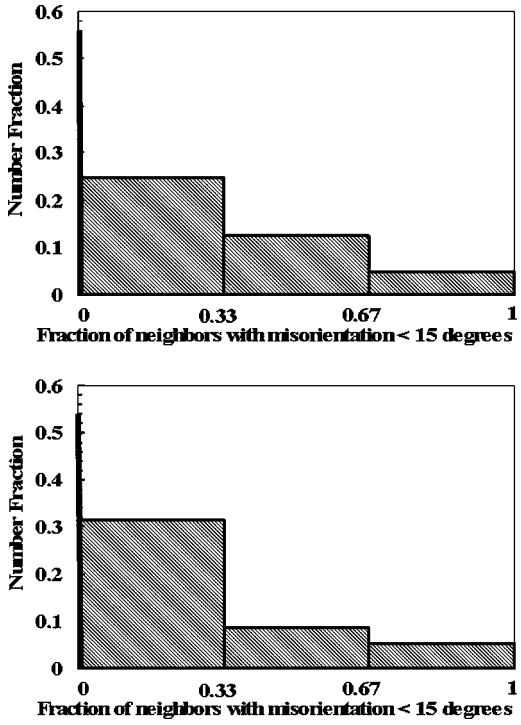

Fig. 6 Histograms of the number fraction of grains as a function of the fraction of their neighbors having a low misorientation (<15 deg): (a) experimental microtexture from OIM; (b) simulated final microtexture with OPAM+MPAM+MTPAM

predominant microtexturing. This motivates a statistically equivalent representation of the microtexture. An iterative microtexture probability assignment method (MTPAM) is used to match the microtexture as discussed in [10]. A set of four statistical bins is set up for the number fraction of grains that have low misorientations with their neighbors (<15 deg). The bins are for (i) none of the neighbors have low misorientation, (ii) between 0% and 33.33% of the neighbors have a low misorientation, (iii) between 33.33% and 66.66% of neighbors have a low misorientation, and (iv) between 66.66% and all of the neighbors have a low misorientation. A histogram of the experimental microtexture is shown in Fig. 6(*a*). In each iteration, the grains, which border a small cluster of similarly oriented grains and have a high misorientation with them are selectively relocated and the cluster is made progressively bigger. Figure 6(*b*) shows the final distribution of fraction of neighbors with low misorientation after simulating with the MTPAM algorithm.

6 Validation of the Ti-6242 Model with Experimental Data

6.1 Mechanical Tests for Validation Study. The crystal plasticity based finite element model of polycrystalline Ti-6242 is validated by comparing with the results of three different types of experiments. These tests, conducted at the Ohio State University and discussed in [7,8,14] are (i) a constant strain rate tension test; (ii) a tension creep test, and (iii) a dwell loading test. The samples for these tests were prepared from Ti-6242 high microtexture forged material. Dog-bone samples were machined for the experiments to dimensions of 1.9 mm thickness, 6 mm width, and 12.7 mm gauge length of the reduced section. The constant strain rate tension test was performed at a strain rate of 1×10^{-4} sec^{-1}. The experimental stress-strain plot for constant strain rate test is shown in Fig. 7. The creep test was performed under stress controlled conditions at a maximum stress of 869 MPa. The creep experiments provide information on plastic strain accumulation with time until failure and this is shown in the strain-time plot of Fig. 8. A change in the slope at nearly 44,640 sec, corresponds to the onset of an internal crack. The primary crack is detected by an in situ ultrasonic method developed in [7,8], in which reflected signals from the cracks are recorded. The dwell test was performed in a stress-controlled mode at a maximum stress of 869 MPa, with 0.0 *R* ratio. The dwell time was 2 min at the maximum stress and the loading-unloading time was 2 sec, with the loading-unloading cycle frequency being 1 Hz. Again, the in situ ultrasonic technique [7,8] was used for monitoring the initiation and propagation of cracks. The dwell experiment provided information on the number of cycles to failure (450 cycles in this test) and the corresponding time.

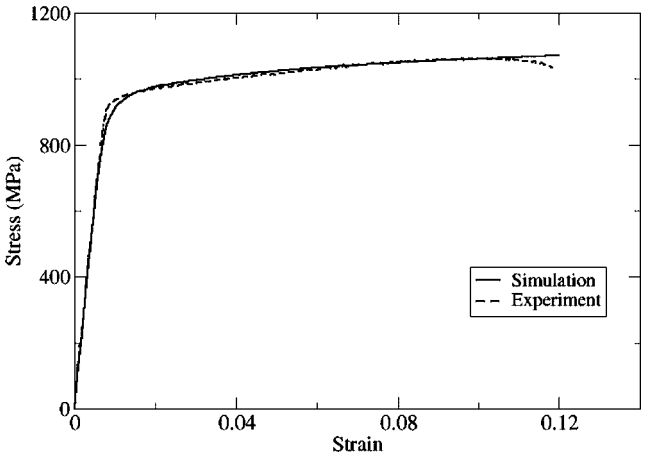

Fig. 7 Validation of the Ti-6242 computational model with experimental results for constant strain rate test

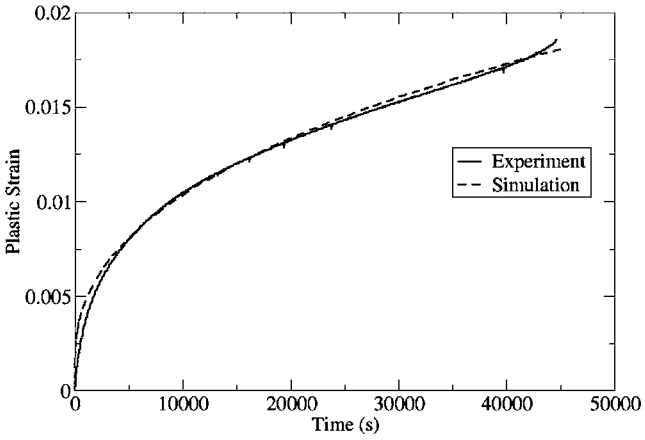

Fig. 8 Validation of the Ti-6242 computational model with experimental results for tension creep

6.2 The FE Model of Polycrystalline Ti-6242. The computational model developed for polycrystalline Ti-6242 alloy is validated with results of the constant strain rate and creep tests discussed in Sec. 6.1. The FE ensemble model of the polycrystalline aggregate consists of a unit cubic domain that is discretized into 2744 eight noded brick elements (type 7) in the commercial finite element code MARC. Each element in the FE model represents a grain with an orientation assigned by the OPAM+MPAM +MTPAM method described in Sec. 5. The number of elements and hence grains yields convergence with respect to the macroscopic response, i.e., adding grains does not change the response. 70% of the grains are primary α which have a hcp crystal structure, and the remaining 30% are transformed β grains represented by the homogenized equivalent model. To simulate the constant strain rate tests, a displacement boundary condition is applied to the top face of the unit cube as

$$u(t) = l_o[\exp(\dot{\varepsilon}_c t) - 1] \tag{13}$$

where l_o is the initial dimension (=1) of the cube and $\dot{\varepsilon}_c$ is the applied strain rate. To simulate the creep experiments, a uniform pressure boundary condition, ramped from zero to the desired creep load in an interval of 1 s is applied to the top face using the FORCEM routine of MARC.

6.3 Validation Results. The average simulated stress-strain responses for the constant strain rate tests are plotted in Fig. 7 and compared with experimental results. The stresses and strains are in the direction of the applied displacement (X_2), and the volumetric averages are defined as

$$\bar{\boldsymbol{\sigma}}_{22} = \frac{\sum_{i=1}^{\text{nel}} \sum_{j=1}^{\text{npt}} (\boldsymbol{\sigma}_{22} \boldsymbol{J})_{ij}}{\sum_{i=1}^{\text{nel}} \sum_{j=1}^{\text{npt}} (\boldsymbol{J})_{ij}}, \quad \bar{\boldsymbol{\varepsilon}}_{22} = \frac{\sum_{i=1}^{\text{nel}} \sum_{j=1}^{\text{npt}} (\boldsymbol{\epsilon}_{22} \boldsymbol{J})_{ij}}{\sum_{i=1}^{\text{nel}} \sum_{j=1}^{\text{npt}} (\boldsymbol{J})_{ij}} \tag{14}$$

where $\boldsymbol{\sigma}_{22}$ and $\boldsymbol{\varepsilon}_{22}$ are the Cauchy stress and the total strain at each integration point of an element and J is the determinant of the Jacobian matrix at these integration points. The total number of elements in the model is nel and npt corresponds to the number of integration points per element. Similarly, the volume-averaged simulated plastic strain is plotted as a function of time and compared with results of the creep experiments in Fig. 8. For both of these experiments, the agreement between experimental and simulated results is excellent.

Table 3 Comparison of the maximum values of basal normal stress, equivalent plastic strain, and stress along loading direction, for the creep and dwell simulations prior to observed failure initiation

	Creep (after 44,640 secs)	Dwell (after 450 cycles)	Percent difference
Basal normal stress σ_n^b (MPa)	1149.56	1173.78	2.1
Equivalent plastic strain	0.0049	0.0055	13.6
Stress along loading direction (MPa)	1226.56	1247.48	1.7

7 Effect of Microstructural Variables on Failure Initiation

It is important to detect potential sites of crack initiation under creep and dwell loading and relate them to the surrounding microstructure to understand the mechanisms of cold dwell fatigue. A combination of experimental observations in [7,8] with microstructural analysis of the results by the experimentally validated computational model is undertaken to identify important variables that are responsible for microscopic damage initiation in polycrystalline Ti-6242 due to creep and dwell loadings. Experimental observations and studies on creep and dwell fatigue in [1,10,12,14] suggest the possibility of the stress normal to the basal planes (basal normal stress), stress in the loading direction or the equivalent plastic strain, as being variables which may contribute to the nucleation of cracks in polycrystalline Ti-6242. The most important variables are identified from a comparative study of the simulation results with creep and dwell fatigue experiments performed in [7,8]. Localizations in stresses and strains at critical grains are sought out as precursors to failure initiation. Subsequently, various microstructural morphology parameters such as orientation and misorientation distributions that may contribute to these localizations are looked into for identifying the critical parameters. Two simulations are carried out with the computation model for this purpose in accordance with the creep and dwell tests mentioned in Sec. 6.1. First is the creep simulation, in which load is ramped from zero to 869 MPa in 1 sec and is then held constant. The load corresponds to approximately 95% of the initial yield strength of the Ti-6242 (see Fig. 7). The creep simulation is continued to approximately 744 min, at which crack initiation was detected by the ultrasonic technique. Next, a dwell simulation with dwell time of 2 min at a controlled stress of 869 MPa with an unload-reload time of 2 sec in each dwell cycle is conducted. The dwell simulation is run for 450 cycles, at which the experimental sample in [7,8] failed.

7.1 Investigation of Evolving Microscopic Variables under Creep and Dwell Loading. As mentioned earlier, the basal normal stress, stress in the loading direction, and the equivalent plastic strain, are the evolving variables which are carefully studied in this example for possible indicators of failure initiation. High basal normal stress $\boldsymbol{\sigma}_n^\tau$ in the primary α grains are often caused by orientations that are unfavorable for easy $\langle a \rangle$ type slip and local load shedding from neighboring softer grains. The stress component $\boldsymbol{\sigma}_n^b$ normal to the basal plane, i.e., along the [0001] axis of the hcp crystal is expressed as

$$\boldsymbol{\sigma}_n^b = \mathbf{n}_b(\boldsymbol{\sigma}\mathbf{n}_b) \tag{15}$$

where $\boldsymbol{\sigma}$ is the Cauchy stress tensor, $\mathbf{n}_b(=\mathbf{F}^{e^{-T}}\mathbf{n_0})$ corresponds to the unit normal vector along the [0001] axis in the global coordinate system at a given time, for which $\mathbf{n_0}$ is the corresponding vector in the initial or reference configuration. The maximum value of $\boldsymbol{\sigma}_n^b$ in a grain for the creep and dwell simulations, just before the onset of failure as discussed in Sec. 6.1, are presented in Table 3. For the dwell simulations, the values correspond to the

Table 4 Values of microstructural parameters θ_c, θ_{max_mis}, and basal normal stress for grains exhibiting high basal stresses in tension creep and dwell

Number	Angle between c axis and loading axis (θ_c) (deg)	Maximum misorientation with neighboring grains (θ_{max_mis}) (deg)	Basal normal stress (MPa)
Grain 1	4.42	84.31	1149.56
Grain 2	13.83	90.99	1116.28
Grain 3	10.85	69.88	1098.26
Grain 4	18.44	64.75	1089.72
Grain 1	4.42	84.31	1173.78
Grain 2	13.83	90.99	1141.35
Grain 3	10.85	69.88	1126.70
Grain 4	9.51	87.88	1120.51

load level just before unloading at the end of dwell cycle. The second row in Table 3 corresponds to the simulated value of the maximum equivalent plastic strain in a grain $\bar{\varepsilon}^p\left(=\sqrt{\frac{2}{3}\left\{\frac{1}{2}(F^p_{ki}F^p_{kj}-\delta_{ij})\right\}\left\{\frac{1}{2}(F^p_{ki}F^p_{kj}-\delta_{ij})\right\}}\right)$, corresponding to the time of observed crack initiation in creep and dwell tests. Finally, the third row corresponds to the maximum value of the normal stress $\boldsymbol{\sigma}_{22}$ in the loading direction.

To seek out which of the three local variables ($\boldsymbol{\sigma}^b_n, \bar{\boldsymbol{\varepsilon}}^p, \boldsymbol{\sigma}_{22}$) is the primary contributor to crack initiation and hence identify the crack initiation mechanism, an assumption is made with respect to these evolving variables. It is proposed that the same value of the local variable should be reached to initiate a crack for both creep and dwell tests, since the initiation will be governed by this value, no matter what is the mechanical test. Consequently, the maximum values of $\boldsymbol{\sigma}^b_n, \bar{\boldsymbol{\varepsilon}}^p$, and $\boldsymbol{\sigma}_{22}$ for the creep and dwell simulations in Table 3 are compared for the least difference. The difference is low for both the stresses ($\sim$2%) whereas it is quite large for equivalent plastic strain by ($\sim$14%). These data suggest that crack initiation in polycrystalline Ti-6242 is possibly stress induced. These results are corroborated by experimental observations in [1] that fracture sites of dwell fatigue specimens of polycrystalline Ti-6242 show little evidence of ductility. Furthermore, Woodfield et al. [9] have observed that α grains always crack at or close to the basal plane and Bache and Evans [28] have mentioned that grains in $\alpha+\beta$ Ti alloys with their basal planes nearly perpendicular to the principal stress axis promote the formation of cleavage facets with a near basal plane orientation. From these observations, it may be concluded that the stress normal to the basal plane is crucial in initiating failure in polycrystalline Ti-6242. In the next sections, microstructural aspects and mechanisms affecting the concentration of this stress is investigated.

Table 5 Values of θ_c, θ_{max_mis}, and basal normal stress for two critical grains exhibiting highest basal normal stresses, one exhibiting a midlevel stress and one exhibiting a low stress in creep and dwell fatigue

		Angle between c-axis and loading axis (θ_c), (deg)	Maximum misorientation (θ_{max_mis}), (deg)	Basal normal stress (Mpa)
Dwell	Critical grain 1	4.42	84.31	1173.78
	Critical grain 2	10.85	69.88	1126.70
	Mid level grain	46.86	61.17	477.00
	Non critical grain	74.26	46.53	51.00
Creep	Critical grain 1	4.42	84.31	1149.56
	Critical grain 2	10.85	69.88	1098.26
	Mid level grain	41.89	62.8	534.36
	Non critical grain	74.26	46.53	58.89

Table 6 Values of θ_c, θ_{max_mis}, and loading direction stress for the grains exhibiting the highest stress in the loading direction in creep

Number	Angle between c axis and loading axis (θ_c) (deg)	Maximum misorientation with neighboring grains (θ_{max_mis}), (deg)	Stress σ_{22} in the loading direction (MPa)
Grain 1	18.45	64.75	1226.55
Grain 2	52.30	90.47	1188.5
Grain 3	84.15	75.99	1180.65
Grain 4	26.64	92.71	1177.85

7.2 Effect of Grain Orientation and Misorientation on Local Stresses. To identify microstructural parameters that induce large local concentrations in the stress $\boldsymbol{\sigma}^b_n$, four grains with high stress values are selected and various parameters are analyzed for sensitivity. From this analysis, two important parameters emerge, viz. (i) the angle between the c axis and the loading axis ($\boldsymbol{\theta}_c$), and (ii) the maximum misorientation ($\boldsymbol{\theta}_{max\_mis}$) of a grain with its neighbors. It is interesting to note that the average misorientation is not found to be as significant in this analysis, which points to the extreme-value postulates on crack initiation. Relevant data for the four grains are presented in Table 4 for creep and dwell. All of these critical grains have low $\boldsymbol{\theta}_c$ ($<$20 deg) and high $\boldsymbol{\theta}_{max\_mis}$ ($>$70 deg). To consolidate this observation, the $\boldsymbol{\sigma}^b_n$ values and the corresponding orientation parameters are studied for two additional grains that have intermediate and low value of basal normal stress. The comparison data for both dwell and creep loading are presented in Table 5. The trend is consistent in this example. Grains with the highest value of basal normal stress have low $\boldsymbol{\theta}_c$ and high maximum misorientation $\boldsymbol{\theta}_{max\_mis}$ and the stresses decrease with higher $\boldsymbol{\theta}_c$ and lower $\boldsymbol{\theta}_{max\_mis}$. Similar values of the parameters are noted for the dwell and creep results in this example. The same trend is observed for the stress $\boldsymbol{\sigma}_{22}$ with respect to misorientation only, as seen in Table 6. The orientation of the c-axis with loading axis is not relevant for the stress in loading direction. On the other hand, it can be seen from Table 7 that the equivalent plastic strain is high for grains with high $\boldsymbol{\theta}_c$ and $\boldsymbol{\theta}_{max\_mis}$. These equivalent plastic strains are much higher than the average plastic strains at failure as shown in Fig. 8. This analysis clearly delineates the basal plane orientation ($\boldsymbol{\theta}_c$) and maximum misorientation ($\boldsymbol{\theta}_{max\_mis}$) as the key parameters that decide crack initiation and should be incorporated in a criterion governing the initiation process.

7.3 Effect of Load Shedding and Stress Redistribution Due to Creep on Local Stresses. This phenomenon in creeping heterogeneous materials has been discussed in [11]. It is relevant in fatigue crack initiation because it yields regions of high stress concentration that are potential nucleation sites. In polycrystalline Ti-6242, with neighboring hard ($\langle c+a\rangle$ oriented grains) and soft ($\langle a\rangle$ oriented grains) grains indicated by larger misorientations, compatibility requirements with additional creep causes the strain near the interface to be higher than that away from it. This gives

Table 7 Values of θ_c, θ_{max_mis}, and equivalent plastic strain for the grains exhibiting the highest strain values in creep

Number	Angle between c axis and loading axis (θ_c) (deg)	Maximum misorientation with neighboring grains (θ_{max_mis}), (deg)	Equivalent plastic strain $\bar{\varepsilon}^p$
Grain 1	66.33	90.28	0.0048
Grain 2	79.40	67.10	0.0045
Grain 3	58.61	86.66	0.0044
Grain 4	81.39	67.10	0.0042

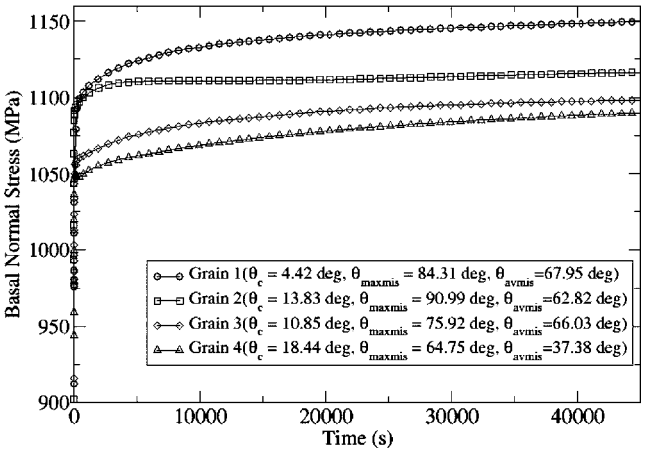

Fig. 9 Evolution of basal normal stress with time for four grains with high σ_n^b in tension creep

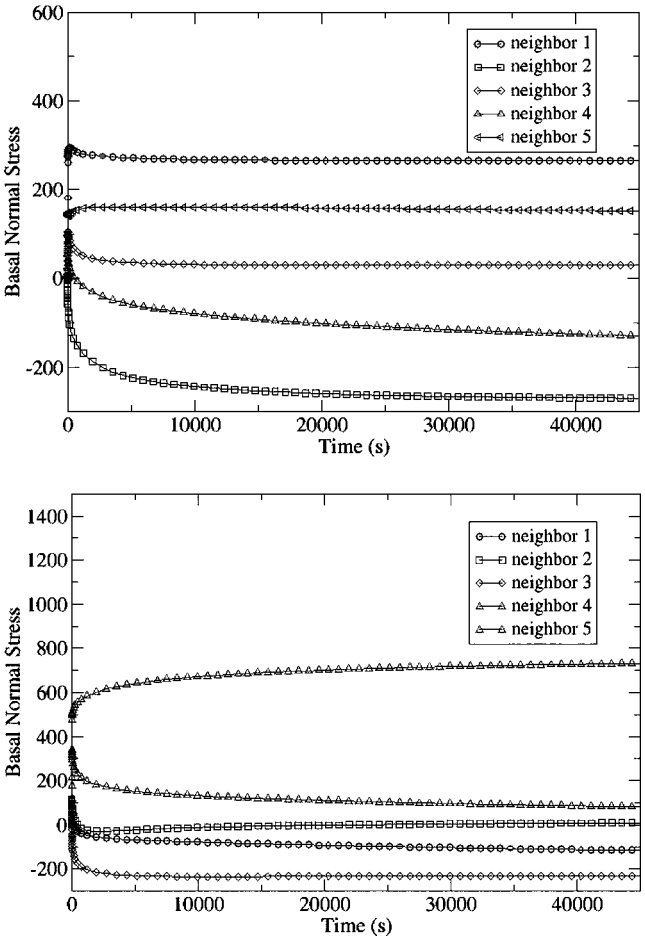

Fig. 10 Evolution of basal normal stress in the neighbors of grains with high basal normal stresses: (a) grain 1 and (b) grain 2 in Fig. 9

rise to a high stress concentration peak in the harder grain and a low stress peak in the softer grain near the interface. With creep and time, the higher and lower stress peaks loft and dip, respectively, to cause larger gradients. This stress redistribution between microstructural regions with different strengths is a fundamental mechanism leading to the nucleation of cracks at or close to the basal plane in the Ti-6242 polycrystals. The evolution of basal normal stresses for four grains with high σ_n^b values is plotted for creep in Fig. 9. The values of σ_n^b for these grains rise with time due to time-dependent load shedding between grains with large orientation mismatches. Load shedding has been shown to increase significantly with the rate sensitivity exponent m in [11]. For this study however, the increase is modest due to the lower value of $m=0.02$. To see the effect of load shedding, the evolution of σ_n^b in all the neighbors of two grains is also plotted in Figs. 10(a) and 10(b). Thefollowing observations are made from these plots.

(i) The time evolution of σ_n^b in the grains with high stress values show that the highest σ_n^b reached is about 1170 MPa, even though the applied stress is only 869 MPa. This corresponds to those grains for which the [0001] or c axis makes an angle of less than ~20 deg with the loading axis. Thus, these are the "hard" grains. The low θ_c results in high $\langle \mathbf{c}+\mathbf{a} \rangle$ activity. As the critical resolved shear stress for $\langle \mathbf{c}+\mathbf{a} \rangle$ slip systems is higher than that for $\langle \mathbf{a} \rangle$ slip systems, the grain experiences a high σ_n^b.

(ii) The evolution of σ_n^b in the neighbors of the above high stressed grains as shown in Figs. 10(a) and 10(b) shows that the stress in most of the neighbors decrease with time. These are the "soft" grains. A few exceptions, where stresses in the neighbors rise are possibly due to load shedding from other adjacent grains.

8 Conclusions

This paper is aimed at identifying important microstructural parameters that play important roles in the failure initiation of polycrystalline Ti-6242 subjected to creep and dwell loading. An experimentally calibrated and validated finite element model, incorporating rate dependent elastocrystal plasticity, is developed for analyzing evolving variables in material microstructure with this aim. The crystal plasticity model, for which material properties are calibrated from tensile and compressive tests on single crystals and colonies, accounts for tension-compression asymmetry and size effects in the polycrystalline microstructure. The Ti-6242 FE model also incorporates a homogenized equivalent model of the transformed β colonies. The polycrystalline FE model is successfully validated by comparing with the results of constant strain rate and creep experiments.

The computational model is consequently used for the identification of possible microstructural variables that may result in local crack initiation. By comparing the local values of these variables at damage initiation for creep and dwell loading, the stress normal to the basal plane in the primary α phase is identified to be a key variable instigating failure in polycrystalline Ti-6242 microstructures. Experimentally, the onset of damage has been detected in associated studies using ultrasonic techniques. The experiments also show that crack nucleates on the basal plane and progresses along this facet.

Next, the aspects of grain orientation and misorientations that cause the high values of the basal normal stresses leading to initiation are analyzed. It is found that grains for which the c axis makes low angles with the loading axis, and for which the maximum misorientation with neighboring grains is high are most susceptible to high stress development. The local basal normal stresses in these grains can reach values that are much higher than the applied load due to high $\langle \mathbf{c}+\mathbf{a} \rangle$ activity combined with load shedding from neighboring grains. Hard grains with low angles between the c axis and loading axis, exhibit increasing basal normal stress while the neighboring soft grains show a decreasing trend due to creep induced load shedding. A key realization from this analysis is the importance of accurate representation of orientation and misorientation distributions, as well as microtexture in the FE model in order to predict the local responses that are criti-

cal to failure. The analyses in this paper form the basis for a comprehensive dwell fatigue initiation criterion incorporating key microstructural variables.

Acknowledgment

The authors are grateful to Professor Jim Williams for his overall guidance and support of this work. They are also grateful to Professor Mike Mills, Professor Stan Rokhlin, and Dr. Vikas Sinha for providing guidance and all the experimental data. This work has been supported by the Federal Aviation Administration through Grant No. DTFA03-01-C-0019 (Program Director: Dr. Joe Wilson). This support is gratefully acknowledged. The authors gratefully acknowledge the software support provided by Dr. Sanjay Choudhry and Dr. Shiva Padmanabhan of MSC MARC. The authors acknowledge the insightful suggestions of Dr. A. Woodfield, Dr. A. Chatterjee, Dr. J. Hall, Dr. J. Schirra, and Dr. M. Savage on various aspects of this work. Computer support by the Ohio Supercomputer Center through Grant No. PAS813-2 is also acknowledged.

References

[1] Sinha, V., Mills, M. J., and Williams, J. C., 2004,"Understanding the Contributions of Normal-fatigue and Static-loading to the Dwell-fatigue in a Near-alpha Titanium Alloy," Metall. Trans. A, **35A**, pp. 3141–3148.
[2] Imam, M. A., and Gilmore, C. M., 1979, "Room Temperature Creep of Ti-6Al-4V," Metall. Trans. A, **10A**, pp. 419–425.
[3] Chu, H. P., 1970, "Room Temperature Creep and Stress Relaxation of a Titanium Alloy," J. Mater., **5**, pp. 633–642.
[4] Odegard, B. C., and Thompson, A. W., 1974, "Low Temperature Creep of Ti-6Al-4V," Metall. Trans., **5**, pp. 1207–1213.
[5] Miller, W. H., Chen, R. T., and Starke, E. A., 1987, "Microstructure, Creep and Tensile Deformation in Ti-6Al-2Nb-1Ta-0.8Mo," Metall. Trans. A, **18A**, pp. 1451–1467.
[6] Bache, M. R., 2003, "A Review of Dwell Sensitive Fatigue in Titanium Alloys: The Role of Microstructure, Texture and Operating Conditions," Int. J. Fatigue, **25**, pp. 1079–1087.
[7] Rokhlin. S., 2005, The Ohio State University, Columbus, OH, unpublished.
[8] Williams, J., Mills, M. J., Rokhlin, S., and Rokhlin, S., 2005, "The Evaluation of Cold Dwell Fatigue in Ti-6242", FAA Report Summary, The Ohio State University, Columbus, OH.
[9] Woodfield, A. P., Gorman, M. D., Corderman, R. R., Sutliff, J. A., and Yamron, B., 1996, "Effect of Microstructure on Dwell Fatigue Behaviour of Ti-6242," *Titanium '95 Science and Technology*, P. A. Blenkinsop, W. J. Evans, and H. M. Flower, eds., The Institute of Materials, London, UK, pp. 1116–1124.
[10] Deka, D., Joseph, D. S., Ghosh, S., and Mills, M. J., 2005, "Crystal Plasticity Modeling of Deformation and Creep in Polycrystalline Ti-6242," Metall. Mater. Trans. A (in press).
[11] Hasija, V., Ghosh, S., Mills, M. J., and Joseph, D. S., 2003, "Modeling Deformation and Creep in Ti-6Al alloys with Experimental Validation," Acta Mater., **51**, pp. 4533–4549.
[12] Norfleet, D., 2005, The Ohio State University, Columbus, OH, unpublished.
[13] Balasubramanian, S., 1998, "Polycrystalline Plasticity: Application to Deformation Processing of Lightweight Metals." Ph.D. dissertation, MIT, Cambridge, MA.
[14] Savage, M. F., 2000, "Microstructural and Mechanistic Study of Low Temperature Creep and Dwell Fatigue in Single Colony alpha/beta Titanium Alloys." Ph.D. dissertation, OSU, Columbus, OH.
[15] Suri, S., Vishwanathan, G. B., Neeraj, T., Hou, D. H., and Mills, M. J., 1999, "Room Temperature Deformation and Mechanisms of Slip Transmission in Oriented Single-Colony Crystals of an α/β Titanium Alloy," Acta Mater., **47**, pp. 1019–1034.
[16] Taylor, G. I., 1938, "Plastic Strain in Metals," J. Inst. Met., **62**, pp. 307–324.
[17] Kalidindi, S. R., Bronkhorst, C. A., and Anand, L., 1992, "Crystallographic Texture Evolution in Bulk Deformation Processing of FCC Metals," J. Mech. Phys. Solids, **40**, pp. 537–569.
[18] Bronkhorst, C. A., Kalidindi, S. R., and Anand, L., 1992, "Polycrystalline Plasticity and the Evolution of Crystallographic Texture in FCC Metals," Philos. Trans. R. Soc. London, Ser. A, **341**, pp. 443–477.
[19] Xie, C. L., Ghosh, S., and Groeber, M., 2004, "Modeling Cyclic Deformation of HSLA Steels Using Crystal Plasticity," J. Eng. Mater. Technol., **126**, pp. 339–352.
[20] Kothari, M., and Anand, L., 1998, "Elasto-Viscoplastic Constitutive Equations for Polycrystalline Metals: Application to Tantalum," J. Mech. Phys. Solids, **46**, pp. 51–67.
[21] Harren, S., Lowe, T. C., Asaro, R. J., and Needleman, A., 1989, "Analysis of Large-Strain Shear in Rate-Dependent Face-Centred Cubic Polycrystals: Correlation of Micro- and Macromechanics," Philos. Trans. R. Soc. London, Ser. A, **328**, pp. 443–500.
[22] MSC-MARC Reference Manuals, 2005, MSC, Software Corporation.
[23] Goldberg, D. E., 1989, "*Genetic Algorithm in Search Optimization and Machine Learning*," Addison Wesley, Boston.
[24] Roundy, D., Krenn, C. R., Cohen, Marvin L., and Morris, J. W., 2001, "The Ideal Strength of Tungsten," Philos. Mag. A, **81**, pp. 1725–1747.
[25] Xie, C. L., and Nakamachi, E., 2002, "The Effect of Crystallographic Textures on the Formability of High-strength Steel Sheets," J. Mater. Process. Technol., **122**, pp. 104–111.
[26] Kumar, A., and Dawson, P. R., 1998, "Modeling Crystallographic Texture Evolution with Finite Elements over Neo-Eulerian Orientation Spaces," Comput. Methods Appl. Mech. Eng., **153**, pp. 259–302.
[27] Kocks, U. F., Tomé, C. N., and Wenk, H. R., 1998, "*Texture and Anisotropy: Preferred Orientations in Polycrystals and Their Effect on Materials Properties*," Cambridge University Press, Cambridge.
[28] Bache, M. R., and Evans, W. J., 2003, "Dwell Sensitive Fatigue Response of Titanium Alloys for Power Plant Applications," J. Eng. Gas Turbines Power, **125**, pp. 241–245.